Journal of
Materials Chemistry C

ROYAL SOCIETY
OF CHEMISTRY

PAPER

View Article Online
View Journal | View Issue

Check for updates

Cite this: *J. Mater. Chem. C*, 2025, **13**, 103

Emergence of heavy-fermion behavior and distorted square nets in partially vacancy-ordered $Y_4Fe_xGe_8$ ($1.0 \leq x \leq 1.5$)†

Hengdi Zhao,[a] Xiuquan Zhou,[a] Mohammad Usman,[a] Ramakanta Chapai,[a] Lei Yu,[b] Jianguo Wen,[b] Hyowon Park,[ac] Alexios P. Douvalis,[d] Patricia E. Meza,[e] Yu-Sheng Chen,[f] Ulrich Welp,[a] Stephan Rosenkranz,[a] Duck Young Chung[a] and Mercouri G. Kanatzidis *[ag]

Disorders in intermetallic systems belonging to the $CeNiSi_2$-family are frequently overlooked. Even compounds presumed to be stoichiometric, such as $YFeGe_2$, can be misidentified. Here, we report a series of $Y_4Fe_xGe_8$ ($1.0 \leq x \leq 1.5$) compounds and show, using high-resolution synchrotron X-ray diffraction, that they feature asymmetrical structural distortions in the Fe and Ge sites that lead to a superstructure with partially ordered Fe vacancies and distorted Ge square-net in the triclinic crystal system, space group $P\bar{1}$ with a = 11.4441(3) Å, b = 32.7356(7) Å, c = 11.4456(3) Å, α = 79.6330(10)°, β = 88.3300(10)°, and γ = 79.6350 (10)°. The unit cell is 16 times the conventional orthorhombic cell with the space group *Cmcm*. We identified the lower and upper limits for Fe in $Y_4Fe_xGe_8$ ($1.0 \leq x \leq 1.5$). Our physical property measurements yielded a Sommerfeld coefficient γ = 39.8 mJ mole^{-1} K^{-2}, a Kadowaki–Woods ratio of 1.2×10^{-5} μΩ cm mole^2 K^2 mJ^{-2}, and a Wilson ratio of 1.83, suggesting heavy fermion behavior in the absence of f electrons, a rather rare case. Furthermore, we observed strong spin frustration and noted findings indicating possible superconductivity associated with the Fe content.

Received 22nd August 2024,
Accepted 25th October 2024

DOI: 10.1039/d4tc03601h

rsc.li/materials-c

Introduction

The $CeNiSi_2$-type structure[1] consists of a wide collection of rare earth or alkaline earth metal (R) transition metal (M) silicides and germanides (X). This structure type comprises two distinct layers: AlB_2-type[2] [RX] and edge-sharing square pyramidal MX_5 slabs. This family further expands its structural diversity with derivatives including non-stoichiometric vacancy disorder on the M site,[3–5] superstructures with vacancy ordering,[6–8] and even homologous series.[9,10] This diversity in intermetallic compounds of the $CeNiSi_2$-family gives rise to rich physics including superconductivity,[3,11] heavy fermion behavior,[12] and new emerging orders induced by pressure, such as superconductivity.[13–15]

A heavy-fermion system features strong correlations between localized magnetic and conduction electrons through the competition of the Kondo effect and the Ruderman–Kittel–Kasuya–Yosida (RKKY) interaction.[16–18] Experimentally, a heavy-fermion metal is characterized by a large Sommerfeld coefficient γ arising from the large density of states near the Fermi level, with a typical value ranging from 20 mJ mole^{-1} K^{-2} to up to 1600 mJ mole^{-1} K^{-2}.[19] Heavy fermion systems are known to host diverse strong correlated phenomena.[19] What is particularly interesting among them is the unconventional superconductivity in the heavy fermion systems, which only appears after the full suppression of an antiferromagnetic phase, suggesting that fluctuations associated with a magnetic quantum critical point play an important role in facilitating superconductivity.[20,21] Interestingly, this behavior mirrors that of Fe-based superconductors,[22] where unconventional superconductivity can manifest by suppressing the magnetism in Fe *via* doping.[23–27] This can be considered one of the strategies for seeking unconventional high-T_c (critical temperature) superconductors as the cuprates[28] also showed interplays between magnetism and superconductivity.[29] Therefore, it is of great

---

[a] Materials Science Division, Argonne National Laboratory, 9700 South Cass Avenue, Lemont, IL 60439, USA. E-mail: m-kanatzidis@northwestern.edu
[b] Center for Nanoscale Materials, Argonne National Laboratory, 9700 South Cass Avenue, Lemont, IL 60439, USA
[c] Department of Physics, University of Illinois Chicago, Chicago, Illinois 60607, USA
[d] Department of Physics, University Ioannina, Ioannina, 45110, Greece
[e] Department of Material Science and Engineering, Northwestern University, Evanston, Illinois 60208, USA
[f] NSF's ChemMatCARS, the University of Chicago, 9700 South Cass Avenue, Lemont, Illinois 60439, USA
[g] Department of Chemistry, Northwestern University, Evanston, Illinois 60208, USA

† Electronic supplementary information (ESI) available. CCDC 2357729 and 2357730. For ESI and crystallographic data in CIF or other electronic format see DOI: **https://doi.org/10.1039/d4tc03601h**

interest to illustrate whether similar behavior can be hosted beyond the Fe–As and Fe–Se systems, such as in the Fe–Ge system.

YFe_2Ge_2, analogous to $KFe_{2-x}Se_2$ (T_c = 35 K),[30] has shown unconventional superconductivity between 1.4–1.8 K,[31–33] which was thought to be related to the magnetism in Fe.[34] Therefore, the $YFeGe_2$ system[35] can be a candidate for hosting unconventional superconductivity due to its close proximity to YFe_2Ge_2. Our previous work has shown that vacancy-ordered Ru-deficient Y_4RuGe_8 in the $CeNiSi_2$-family exhibits superconductivity below 1.3 K.[8] Although the synthesis of stoichiometric $YFeGe_2$ was reported,[35] its physical properties or the Fe-deficient phases have not been studied. In addition, adjusting the Fe content in this system can be used to tune the Fermi level to induce emerging properties. Therefore, in this work, we report a series of new compounds with the composition of $Y_4Fe_xGe_8$ ($1 \leq x \leq 1.5$) crystallizing in a structure related to the $CeNiSi_2$-type with a distorted Ge square-net and partially vacancy-ordered superstructure. Furthermore, we characterized the heavy fermion state of $Y_4Fe_xGe_8$ through measurements of electrical transport, heat capacity, and magnetic susceptibility. The extracted Sommerfeld coefficient γ = 39.8 mJ mole^{-1} K^{-2}, the Kadowaki–Woods ratio of 1.2×10^{-5} μΩ cm mole^2 K^2 mJ^{-2}, and the Wilson ratio of 1.83, all fall within the typical range of a heavy fermion system. While heavy fermion behavior typically necessitates the presence of f-electrons, discovering instances where this phenomenon arises without them is both rare and fascinating, defying conventional expectations. The first notable exception containing only 3d electrons is the transition metal vanadate, LiV_2O_4,[36] and its heavy-fermion behavior is attributed to some non-Kondo mechanism, such as strong AFM spin fluctuations due to geometrical spin frustration.[37–42] In addition to LiV_2O_4, only a few more exemptions involving 3d/4d electrons have been reported in transition-metal oxides, such as $CaCu_3Ru_4O_{12}$,[43] $Ba_4Nb_{1-x}Ru_{3+x}O_{12}$;[44] chalcogenides, for instance, Fe_3GeTe_2,[45] KNi_2Se_2;[46] ferromagnetic superconducting Laves metal $ZrZn_2$,[47,48] 1T/1H-TaS_2 heterostructure,[49,50] $MoTe_2$/WSe_2 moiré lattice,[51] and Fe-based strongly-correlated intermetallic.[52–54] The heavy fermion behavior was also theoretically proposed in twisted trilayer graphene[55] and magic-angle twisted bilayer graphene.[56,57] In addition to the heavy fermion behavior, strong spin frustration and a possible superconducting state in $Y_4Fe_xGe_8$ will also be discussed.

Experimental section

General details

Iron powder (Alfa Aesar, 99.998%) and yttrium powder (Lunex, 99.98%) were used as received. Germanium pieces (Plasmaterials, 99.999%) were ground to a fine powder prior to use. Indium shots (Apache Chemicals, 99.999%) were briefly rinsed with dilute HCl to remove a thin layer of oxide impurities on the surface. The handling of all materials was performed in an M-Braun glovebox under an inert Ar atmosphere with O_2 and H_2O levels below 0.1 ppm.

Synthesis

$Y_4Fe_xGe_8$ ($1.0 < x < 1.5$) crystals were grown from molten In. It is advisable to use Y powder rather than chunks or pieces to subdue the formation of Y/Ge binaries. A stoichiometric mixture of Y/Fe/Ge containing 0.25 g of Y, 0.0565 g of Fe, and 0.41 g of Ge was layered under ∼6 g of In flux in an alumina crucible. The alumina was capped with a stainless-steel frit held in place by a quartz support for hot filtration. This assembly was sealed in a 15 mm OD and 13 mm ID fused silica tube evacuated under a 10^{-4} mbar vacuum. The ampoule containing the charge was placed in a furnace heated at 30 °C h^{-1} to 1100 °C, dwelled there for 12 h, cooled at 2 °C h^{-1} to 1000 °C, cooled at 5 °C h^{-1} from 1000 °C to 800 °C, cooled at 15 °C h^{-1} from 800 °C to 500 °C, where the ampoule was carefully taken out of the furnace and centrifuged at 2000 rpm for 30 s to separate the crystals from molten In flux. Rod-shaped crystals with the long dimension beyond 3 mm in length were obtained with granular residues on their surface which were removed by soaking the crystals in dilute HCl (4 parts of water to 1 part of conc. HCl) overnight followed by washing them thoroughly with water and acetone. $Y_4Fe_xGe_8$ samples with variable x were also prepared using direct combination reaction of the respective elements at 1000–1100 °C, followed by a furnace cooling by turning off the furnace and letting it cool naturally. The direct combination samples were homogenized with intermediate grind and checked with powder X-ray diffraction until a uniform solid solution is reached.

Diffraction

Powder X-ray diffraction (PXRD) data were collected using a Rigaku Miniflex X-ray diffractometer with Cu Kα radiation, λ = 1.5406 Å. Laboratory single crystal XRD data were collected using a STOE IPDS diffractometer or Bruker APEX-2 diffractometer with Mo Kα radiation at room temperature. Synchrotron X-ray beam single crystal XRD data were collected at 15-IDD (NSF's ChemMatCARS at the Advanced Photon Source) with a wavelength λ = 0.41328 Å at either room temperature or under liquid nitrogen flow (∼100 K). Single-crystal structures were solved with the ShelXT intrinsic phasing solution method[58] and were refined with ShelXL full-matrix least-squares minimization on F^2 method[59] using Olex2[60] as the graphical interface.

Electron microscopy

Microscopic images were examined on a Hitachi SU-70 SEM field emission scanning electron microscope (SEM), and their elemental compositions were determined by energy dispersive X-ray spectroscopy (EDS) using a BRUKER EDS detector. Transmission electron microscopy (TEM) images and electron diffraction patterns were obtained using the Argonne Chromatic Aberration-corrected TEM (ACAT), which is an FEI Titan 80–300 ST equipped with an image corrector to correct both spherical and chromatic aberration to enable information resolution better than 0.08 nm at 200 keV. TEM samples were prepared by mechanical grinding of single crystals of $Y_4Fe_{1.5}Ge_2$ using mortar and pestle, followed by spreading smaller particles onto a copper TEM grid.

X-ray photoelectron spectroscopy (XPS)

X-ray photoelectron spectroscopy measurements (XPS) were performed using a Thermo Scientific Nexsa G2 system (monochromated Al Kα radiation, ∼1486.6 eV) at a pressure of $\sim 6.4 \times 10^{-7}$ mbar and with an analysis spot size of 50 μm. Samples were charge compensated with a flood gun. To prepare samples for XPS oxidation state analysis and remove surface contamination without Ar beam sputtering, the $Y_4Fe_xGe_8$ particles were washed with 1 : 4 parts by volume HCl : DI water for 10 minutes. All peaks were charge-corrected to adventitious carbon at 284.8 eV. Peak widths were not allowed to be larger than 3.5 eV.

Mössbauer spectroscopy

^{57}Fe Mössbauer spectra (MS) of a fine powder $Y_4Fe_xGe_8$ sample resulted from grinding several crystals in an agate mortar were collected in transmission geometry at room temperature (RT = 300 K) and 11 K using a constant-acceleration spectrometer, equipped with a ^{57}Co(Rh) source kept at RT, in combination with a closed loop gas He Mössbauer cryostat (ARS). Metallic α-Fe at RT was used for the velocity calibration of the spectrometer and all isomer shift (IS) values are given relative to this standard. The experimentally recorded MS were fitted and analyzed using the IMSG code.[61]

Specific heat

Heat capacity measurements from 1.8 to 300 K were performed in a Quantum Design Dynacool Physical Property Measurement System (Dynacool-PPMS). A sample puck with the appropriate amount of Apiezon N grease was first measured as the background. The sample heat capacity was measured afterward by mounting one bar-shaped single crystal (3 mg in weight) on top of the sample puck. The measurement was performed using a time relaxation method.

Electrical resistivity

Electrical resistivity measurements from 1.8 K to 300 K were performed in the same Dynacool-PPMS system. We employed a Bluefors LD400 dilution refrigerator for low-temperature magneto-transport measurements. This cryostat is equipped with a -bottom-loading sample transfer system and a 9-1-1 T three-axis magnet, and it reaches sample temperatures as low as 25 mK. The standard four-leads method was used for the electrical transport measurement and the DuPont 4929N-100 silver paint was used to bond gold wires to the sample to ensure optimal electrical and mechanical contacts. A bar-shaped single crystal with the dimension of $2 \times 0.3 \times 0.2$ mm^3 was used in the electrical transport measurements.

Magnetic susceptibility

The dc-magnetic susceptibility measurements from 1.8 K to 300 K were performed in a superconducting quantum interference device (SQUID) from Quantum Design Magnetic Property Measurement System (MPMS-3). Multiple coaligned bar-shaped single crystals with a total weight of 14.5 mg were used in the magnetic susceptibility measurements shown in the main text and polycrystalline samples were used for the direct combination measurements shown in the ESI.†

Result and discussion

Crystal structure

Similar to $YFeGe_2$, the Fe-deficient $Y_4Fe_xGe_8$ crystallizes in the orthorhombic space group *Cmcm* (Fig. 1a and b) with a = 4.1384(2) Å, b = 15.8468(8) Å and c = 4.0178(2) Å for x = 1.44(1), equivalent to a Fe occupancy of 0.360(3) for the $CeNiSi_2$-type (Table 1). A similar ratio of Y : Fe : Ge ≈ 4 : 1.5 : 8 was also confirmed by elemental analysis using energy dispersive X-ray spectroscopy (EDS) as shown in Fig. S1 (ESI†). However, upon a closer examination of the diffraction data, we found a large number of reflections were omitted using the orthorhombic symmetry (4690 reflections in orthorhombic *vs.* 23 168 reflections collected in triclinic, hence 80% of reflections were omitted). Therefore, we report here a more accurate crystal structure refinement using the space group $P\bar{1}$ with a = 5.7716(3) Å, b = 8.1916(4) Å, c = 11.5363(5) Å, α = 79.5610(10)°, β = 88.3050(10)°, and γ = 79.5490(10)° in column 3 of Table 1. The refinement of this triclinic cell, two times the volume of the orthorhombic cell, showed meaningful differences in the Ge square-net and Fe layers of the structure as illustrated in Fig. 2a and b for the space groups *Cmcm* and $P\bar{1}$, respectively. A stepwise symmetry reduction caused by Ge and Fe is illustrated in Fig. S2 (ESI†) to show how the ideal orthorhombic space group *Cmcm* transitions to $P\bar{1}$.

In the orthorhombic setting, the Ge square-net undergoes a minor distortion from 90° to 88.285° with a Ge–Ge distance of 2.88450(11) Å; while for the triclinic setting, without any symmetry restrictions, the Ge square-net distort further from rhombi to irregular quadrilaterals resulting in four distinct Ge–Ge distances (Fig. 2b) for each Ge and its four nearest neighbors varying from 2.872(3)–2.901(3) Å, breaking all mirror and glide planes of the space group *Cmcm*. For the Fe layer, despite only slight variations of Fe occupancies from 0.320(7) to 0.394(9) in the triclinic setting, the Fe atoms shift to off-center sites. Moreover, their thermal displacement parameters exhibit significant elongations along diagonals of the *ac*-plane; while they resemble flattened spheres along the *b*-axis in the orthorhombic setting. This suggests that the radius of Fe is too

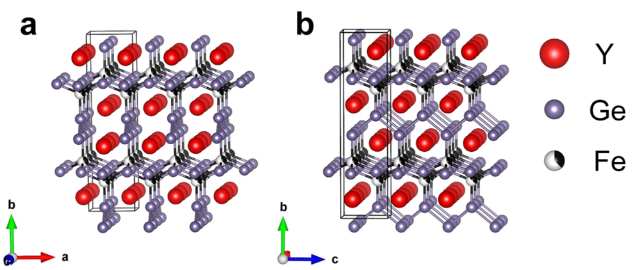

Fig. 1 Crystal structures of $Y_4Fe_xGe_8$, crystallizing in a $CeNiSi_2$-type structure (space group *Cmcm*) viewing at (a) the *ab*-plane and (b) the *bc*-plane.

Table 1 Single crystal refinement data for $Y_4Fe_xGe_8$ ($x = 1.44$) collected using a lab X-ray source in the orthorhombic space group *Cmcm* (column 2) and triclinic space group $P\bar{1}$ (column 3). More detailed report of the crystal structure can be found in Tables S1 and S2 (ESI) and CCDC (CSD2357729 and CSD2357730)†

Empirical formula	$Y_4Fe_{1.44}Ge_8$	$Y_4Fe_{1.44}Ge_8$
Crystal system	Orthorhombic	Triclinic
Space group	*Cmcm*	$P\bar{1}$
Crystal shape and color	Metallic silver	Metallic silver
Unit cell dimensions (Å)	a = 4.1384(2)	a = 5.7716(3)
	b = 15.8468(8)	b = 8.1916(4)
	c = 4.0178(2)	c = 11.5363(5)
α	90°	79.5610(10)°
β	90°	88.3050(10)°
γ	90°	79.5490(10)°
Volume (Å^3)	263.49(2)	527.49(4)
Wavelength (Å)	0.71073	0.71073
Z	1	2
Density (g cm^{-3})	6.408	6.400
Independent reflections	255 [R_{int} = 0.0298]	4508 [R_{int} = 0.0532]
Data k/restraints/parameters	255/0/19	4508/0/150
Goodness-of-fit	1.135	0.946
Final R indices [$I > 2\sigma(I)$]	R_{obs} = 0.0138, wR_{obs} = 0.0293	R_{obs} = 0.0307, wR_{obs} = 0.0749
R indices [all data]	R_{all} = 0.0150, wR_{all} = 0.0298	R_{all} = 0.1473, wR_{all} = 0.1091

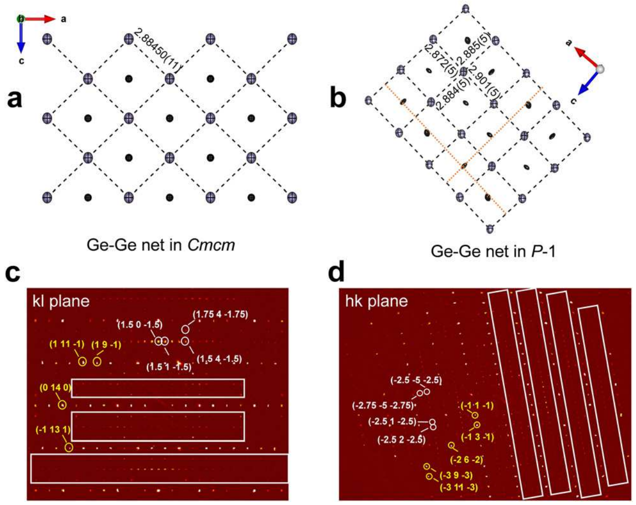

Fig. 2 Comparison of the square-net of the Ge layer in $Y_4Fe_xGe_8$, with the (a) orthorhombic (*Cmcm*) and (b) larger triclinic ($P\bar{1}$) space groups identified from data collected using a lab X-ray source, and precession images of the (c) *kl*-plane and (d) *hk*-plane reflections for a $Y_4Fe_xGe_8$ crystal collected with high-resolution single crystal diffraction at a synchrotron source using a triclinic cell ($P\bar{1}$) of a = 11.4441(3) Å, b = 32.7356(7) Å, c = 11.4456(3) Å, α = 79.6330(10)°, β = 88.3300(10)°, and γ = 79.6350 (10)°. The Ge–Ge distances are shown in (a) and (b) as Angstroms (Å). Ge and Fe atoms are shown as ellipsoids for their thermal displacements in (a) and (b). Selected reflections from the orthorhombic unit cell are circled and labeled in yellow and supercell reflections are shown as white circles or enclosed by white boxes. The dotted lines show Fe moving from the center of each distorted square formed by the nearest Ge atoms.

large to allow full occupancy of the square pyramidal centers in the typical $CeNiSi_2$-type structure.

In comparison, Ru in Y_4RuGe_8[8] is large enough to cause more pronounced distortions to the Ge square-net leading to chessboard-like patterns with each big square of Ge (3.22–3.24 Å) surrounded by four neighboring smaller highly distorted squares (2.53–2.55 Å). As a result, Ru can only occupy square-pyramidal centers enclosed by big squares leaving neighboring Ru sites completely unoccupied. In Y_4RuGe_8, the large Ru atoms cause significant Ge square-net distortions, preventing other Ru atoms from occupying adjacent square pyramidal sites. In contrast, Fe atoms form partially ordered vacancies. While Fe atoms also distort the Ge square-net when occupying square pyramidal sites, their smaller size compared to Ru results in a less pronounced distortion (2.872(3)–2.901(3) Å). This reduced distortion does not completely exclude other Fe atoms from adjacent squares, leading to partially ordered Fe vacancies and off-centering of Fe atoms, which breaks all mirror and glide planes in the orthorhombic space group *Cmcm*. Consequently, in the orthorhombic space group *Cmcm*, the occupancies for Fe sites increase up to 0.375, which corresponds to $Y_4Fe_{1.5}Ge_8$ compared to 0.25 in Y_4RuGe_8, leading to the partial order of Fe vacancies in $Y_4Fe_xGe_8$ ($1.0 \leq x \leq 1.5$). Compared to the disorder in the Ge square-net and Fe layers, there are no meaningful differences between the two space groups for the Y atoms and Ge–Ge zig-zag chains. The Ge–Ge bond distances in the Ge–Ge zig-zag chains are 2.6053(7) Å and 2.601(5)–2.608(4) Å for the orthorhombic and triclinic settings, respectively.

To fully verify the partial order of Fe vacancies in $Y_4Fe_xGe_8$ with asymmetrical distortions and a distorted Ge square-net, we conducted high-resolution single crystal diffraction on a similar sample using a synchrotron X-ray source (15-IDD at APS) at 100 K. Although we were able to index an orthorhombic unit cell similar to the one shown in Table 1, extra reflections from a triclinic supercell were also indexed as a = 11.4441(3) Å, b = 32.7356(7) Å, c = 11.4456(3) Å, α = 79.6330(10)°, β = 88.3300(10)°, and γ = 79.6350 (10)°, whose volume is 16 times of the smaller orthorhombic cell (Table S3, ESI†). Hence, we have discovered a new triclinic cell that surpasses the size of the above-described triclinic cell. Compared to the smaller triclinic cell, the lattice constants of this bigger cell double a and quadruple *b*, leading to a 2 × 4 × 1 supercell. This indicates that the prior refinement overlooked further weak Bragg reflections, which we were able to uncover through synchrotron diffraction. We synthesized precession images from this data collection, and weaker reflections of supercell are clearly seen in the reciprocal lattice that cannot be accounted for using the orthorhombic cell alone, Fig. 2c and d. These extra reflections showed non-integer numbers, usually at $\frac{1}{2}$ and $\frac{1}{4}$, for H and L indices, suggesting a 2 × 4 supercell in the basal plane of *ac* compared to the orthorhombic cell. The refinement of the synchrotron data showed further disparities between the occupancies of the Fe sites ranging from 0.08(2) to 0.475(16), whereas the range is between 0.320(7) to 0.385(8) for the smaller triclinic cell. Therefore, this superstructure is likely a result of partial Fe-vacancy ordering.

To fully understand such disorder in $Y_4Fe_xGe_8$, we conducted a local structural analysis on nanoscale using high-resolution transmission electron microscopy (HRTEM). Based on the atomic resolution image depicted in Fig. 3a, we were able to match the overall atomic positions in the unit cell easily. However, upon closer examination of the periodicity of the Fe atoms, we discovered an imperfect recurrence of Fe atoms in almost every three vacant sites (Fig. 3b). In addition, such repeat is not precise and lacks long-range periodicity (Fig. 3c). This is further confirmed by electron diffraction along the [101] zone axis (Fig. 3d and e), where superstructure reflections similar to those shown in Fig. 2d and e could be seen. All this evidence suggests that $Y_4Fe_xGe_8$ does not exhibit long-range vacancy ordering like Y_4RuGe_8,[8] but instead, Fe creates local disorders leading to asymmetric distortions in the structure. This explains the larger triclinic cells observed that can better account for the structure distortion.

Variation in Fe composition

Although we have seen the spread of *x* in obtained crystals from $x = 1.23(6)$ to 1.49(1), it is unclear what synthetic conditions led to these differences. Therefore, we carried out direct combination reactions to target different nominal *x* values from 0.25 to 2.50 by direct reactions of elemental Y, Fe, and Ge at 1000–1100 °C. We performed Rietveld refinement for as-recovered powder samples as shown in Fig. 4a. For the nominal $x = 0.25$, the sample contained a large number of impurities with less than half being $Y_4Fe_xGe_8$ (17% Ge, 41% $YGe_{1.86}$, and other unidentified impurities). This was not caused by inadequate reaction as less $Y_4Fe_xGe_8$ (∼24% *vs.* 42%) was obtained after further homogenization by grinding and subsequent annealing at 1000 °C for two days. More $YGe_{1.86}$ and YFe_2Ge_2 were obtained from further annealing. However, the purity significantly improved for nominal $x = 0.50$ as we obtained about 90% $Y_4Fe_xGe_8$ with about 10% Ge and an unidentified impurity. Similarly, for $x = 0.75$ and 1.00, we obtained over 90% of $Y_4Fe_xGe_8$ with 8–10% of Ge without the 2nd impurity phase. However, for $x = 1.50$–2.50, we obtained mainly $Y_4Fe_xGe_8$ (∼90%) but with an impurity phase of Y_2O_3. Our *in situ* diffraction studies of ground $Y_4Fe_xGe_8$ crystals loaded in a quartz tube also resulted in Y_2O_3 at higher temperatures. This suggests that Y_2O_3 formed from the reaction of $Y_4Fe_xGe_8$ with quartz ampoules.

Because of the quality of the PXRD data, our Rietveld refinement cannot distinguish small changes in *x* values as the contributions to the form factor from small variations in Fe is small compared to background noise. However, the trend in unit cell volume determined from our refinement is more reliable. Therefore, we used our single crystal data to obtain *x* as a function of volume (*V*) and then used Vegard's law to fit the *x* values (Table 2). We found the actual *x* values varied from 1.021(31) to 1.325(40) despite their nominal values changed from 0.25 to 2.50. There appears to be both lower and upper limits for the Fe content based on the fitted volume data. For the smallest nominal $x = 0.25$, we saw the largest amounts of impurities including unreacted Ge. With increasing nominal *x*, the fitted *x* values tend to increase, but appeared to be saturated below $x = 1.4$. This is consistent with our single crystal data, as we generally obtained crystals with *x* varying from 1 to 1.5. Therefore, we believe that the stoichiometric $YFeGe_2$ reported in literature[35] is likely to be an Fe deficient phase

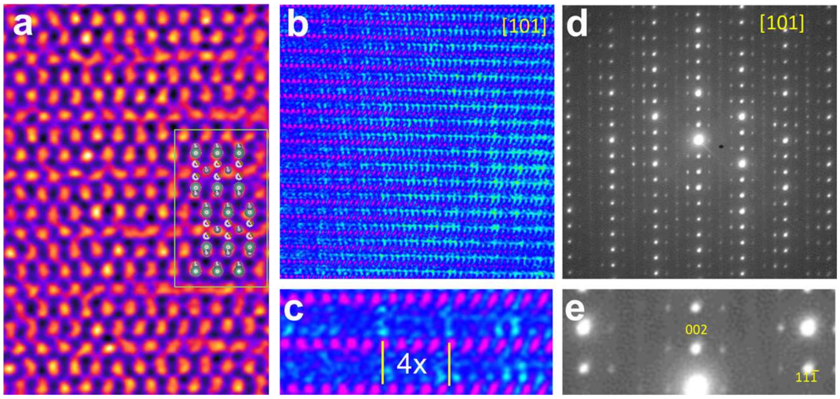

Fig. 3 High-resolution transmission electron microscopy (HR-TEM) images of $Y_4Fe_xGe_8$ showing (a) atomic arrangements of the atoms corresponding to the unit cell, (b) superstructure of Fe showing along the [101] zone axis, (c) zoom of (b) showing Fe repeating after every 4 unit, indicating a 4× unit cell along the (100) direction, (d) electron diffraction of (b) along the [101] zone axis and (e) zoom of (d).

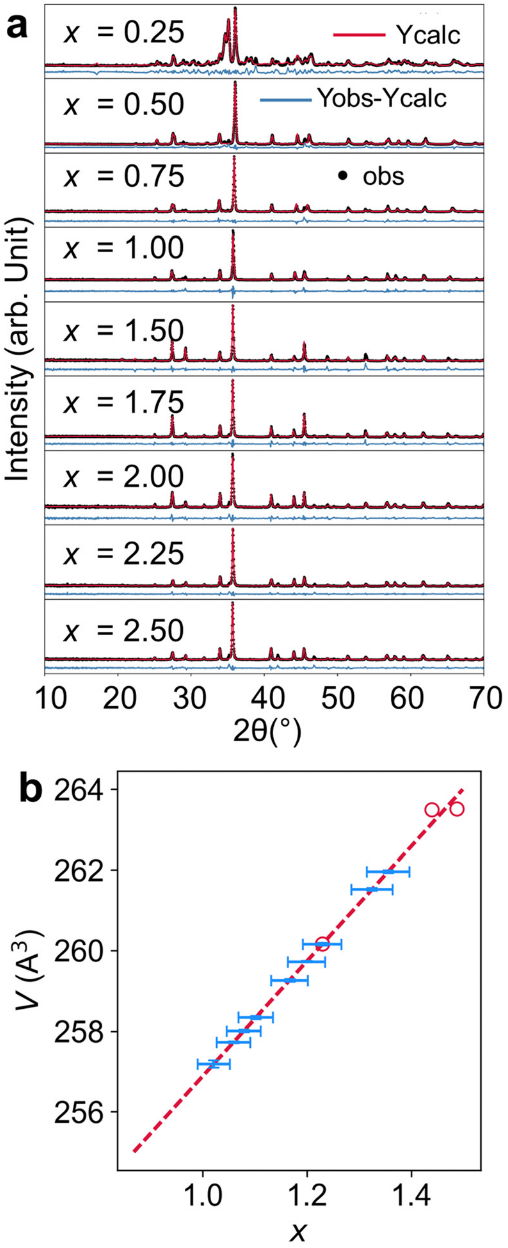

Fig. 4 Analysis of direct combination reaction by (a) Rietveld refinement of the PXRD patterns with nominal ratios of x varying from 0.25 to 2.50 and (b) calculated x (blue) based on the fitted x *vs.* volume modeled from single crystal data (red circle) for each pattern shown in (a). The results are described in Table 2.

since the reported volume is 261.69 Å^3, corresponding to approximately x = 1.34 instead of 4. This is consistent with the upper limit we obtained from our solid-state reactions. Therefore, this evidence demonstrates that the previously reported stoichiometric $YFeGe_2$ was indeed a phase deficient in iron, similar to ours.

Fe oxidation state

To fully understand the oxidation state of Fe we used ^{57}Fe Mössbauer spectroscopy. The ^{57}Fe MS of the $Y_4Fe_xGe_8$ powder sample recorded at RT and 11 K are shown in Fig. 5. These spectra present only quadrupole split contributions, while there is no apparent magnetically split contribution down to 11 K. Although there is no significant change in the shape of the MS between 300 K and 11 K, the spectra possess some broadening and a slight intensity asymmetry in their resonant lines. Thus, one quadrupole split doublet was used to fit both spectra, while an asymmetrical spreading (ΔQS, Gaussian-type) of its quadrupole splitting (QS) values around the central QS^C value was allowed. The resulting Mössbauer parameters are listed in Table 3.

From this table, it is evident that the IS values for the Fe atoms in $Y_4Fe_xGe_8$ lie in the range of the values found for crystalline intermetallic as well as amorphous Fe–Ge alloys,[62] while the temperature evolution of the IS values between RT and 11 K falls within the expected limits due to the second order Doppler shift.[63]

The Mössbauer spectroscopy hyperfine parameters values of IS, $\Gamma/2$, QS^C, asymmetric ΔQS and intensity of spectral resonant lines indicate that there is only one type of neighbor chemical environment for the iron atoms, although this environment involves a slight distribution that could be related to the kind of quasi periodic occurrence of Fe atoms discussed earlier in the crystal structure of $Y_4Fe_xGe_8$, as demonstrated by our diffraction (Fig. 2) and electron microscopy data (Fig. 3).

In this crystal structure, the iron atoms occupy square pyramidal positions with 5 Ge atoms as first neighbors. Each pyramid shares its 4 common base-square edges with other 4 neighboring pyramids, while the position of the fifth ''apex-Ge'' atom in these pyramids is such that the ''orientation'' of each pyramid is opposite to its first 4 basal-square neighboring pyramids and same with its second 4 neighbor pyramids along the diagonals of the base. So the main interaction of iron is with Ge atoms, along which they seem to form a layered-type structure of orientation-alternating $FeGe_5$ pyramids.

As the Fe : Ge ratio in the $Y_4Fe_xGe_8$ phase is 0.18 : 1 it seems rational to seek resemblance with a Fe–Ge crystalline phase with low iron content as for example in $FeGe_2$, which adopts a tetragonal crystal structure and acquires antiferromagnetic ordering for the iron atoms below $T_N \approx 287$ K.[64,65] The IS values of $FeGe_2$ are quite similar to the ones determined for $Y_4Fe_xGe_8$ in this work, indicating a possible resemblance of the electronic configuration for the iron atoms in the latter

Table 2 Calculated x in $Y_4Fe_xGe_8$ synthesized by direct combination reaction of the respective elements. The x value was fitted by Vegard's law from x and volume (V) obtained using single crystal X-ray diffraction

Nominal x	0.25	0.50	0.75	1.00	1.50	1.75	2.00	2.25	2.50
V	257.19	257.73	258.01	259.72	258.34	259.26	260.16	261.95	261.52
Calculated x	1.02(3)	1.06(3)	1.08(3)	1.20(4)	1.10(3)	1.17(4)	1.23(4)	1.36(4)	1.33(4)

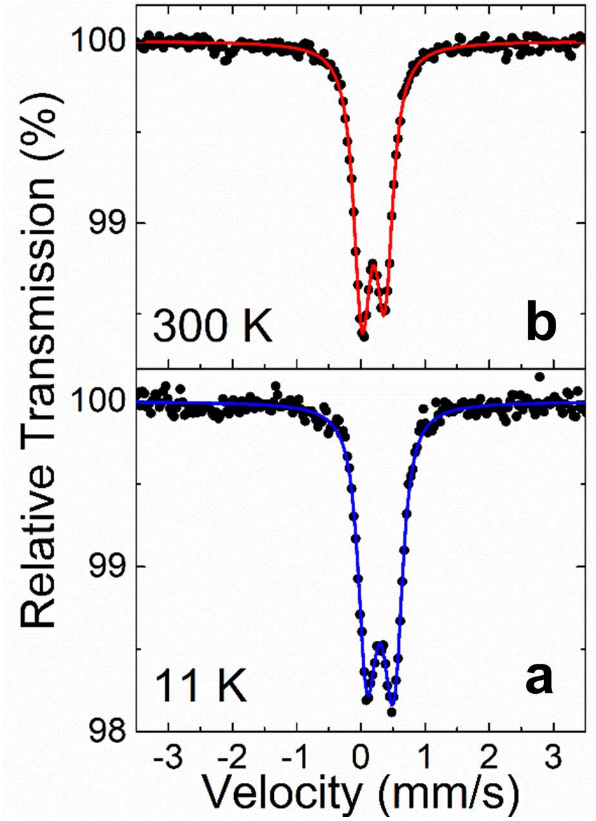

Fig. 5 Mössbauer spectra of ground $Y_4Fe_xGe_8$ crystals recorded at (a) 11 K and (b) room temperature (300 K). The points correspond to the experimental data and the continuous lines to the fitting model.

Table 3 Mössbauer spectroscopy hyperfine parameters values as resulting from the best fits of the corresponding spectra: IS is the isomer shift (relative to α-Fe at room temperature), $\Gamma/2$ is the half line width, QS^C is the central value of the quadrupole splitting and ΔQS is the asymmetric spreading of QS in lower/higher values relative to QS^C. The 300 K and 11 K results are presented in the upper and lower row respectively. Typical estimated uncertainties are ±0.02 mm s^{-1} for IS and $\Gamma/2$, and ±0.01 for QS^C

IS (mm s^{-1})	$\Gamma/2$ (mm s^{-1})	QS^C (mm s^{-1})	$\Delta QS < QS^C/\Delta QS > QS^C$ (mm s^{-1})
0.30	0.13	0.36	0.06/0.04
0.41	0.13	0.42	0.10/0.05

compound to the former. This configuration is thus referred to as an alloying (Fe^0) state.

However, since there is no apparent magnetic transition between RT and 11 K for $Y_4Fe_xGe_8$, we could seek a closer resemblance in the Mössbauer spectroscopy hyperfine parameters of iron in this compound with those found in amorphous Fe–Ge compounds of similar compositions. Indeed, the IS, QS^C, and ΔQS values resulting from $Y_4Fe_xGe_8$ are quite similar to those found for amorphous Fe–Ge compounds in the range of stoichiometries that includes the 0.18 : 1 Fe : Ge ratio throughout the total temperature interval between 11 K and RT.[62,66,67] Moreover, in these reports there is an important additional experimental result that renders increased resemblance with the current studied $Y_4Fe_xGe_8$ phase, which refers to the vanishing magnetic moment of the iron atoms, that is found only for a certain range of low iron concentration and only in the amorphous Fe–Ge system, not the crystalline one. This behavior for the amorphous Fe–Ge compounds is likely associated with the disorder of Fe atoms in the structure akin to that in $Y_4Fe_xGe_8$. It was proposed to be associated with the widening of the 3d band of Fe atoms and its strong hybridization with the sp bands of the underlying Ge atom matrix (for relatively low to medium iron atomic concentrations of Fe_xGe_{1-x}, x = 0.01–0.5).

X-ray photoelectron spectroscopy (XPS) measurements were also conducted to determine the oxidation state of Fe in $Y_4Fe_xGe_8$. The individual samples were washed in an HCl solution to clean the surface of oxidized Fe species, eliminating the need for Ar sputtering. The Fe 2p spectrum in Fig. S4 (ESI†) shows two spin–orbit doublets ($2p_{3/2}$ and $2p_{1/2}$). Although the Fe surface signal is noisy without surface sputtering, only one peak contribution is identifiable for both components. The peak is centered at 707.1 eV and 719.8 eV for $2p_{3/2}$ and $2p_{1/2}$, respectively.[68–70] Studies on FeGe films and other Fe systems conclude that this peak energy corresponds to metallic Fe.[70–72]

Heavy fermion behavior

$Y_4Fe_xGe_8$ is a paramagnetic metal at high temperatures before a superconducting-like transition dominates, which will be discussed later. The magnetic susceptibility at high temperatures is well fitted by a Curie–Weiss law for both crystallographic directions (Fig. 6a). The fits yield a Curie–Weiss temperature, θ_{CW}, and an effective moment, μ_{eff}, for $H//a$ and $H//bc$ of −55.8 K, $0.87\mu_B$ per f.u. and −63.1 K, $1.03\mu_B$ per f.u., respectively with a temperature-independent term χ_0 = 0.0011 emu $mole^{-1}$. The low value of the effective moment is consistent with our results from ^{57}Fe Mössbauer spectroscopy, which is attributed to the strong p–d orbital hybridization between the adjacent Fe and Ge atoms and commonly seen in transition metal intermetallic compounds. However, the system is also strongly correlated, as suggested by the strong antiferromagnetic interactions signaled by the large value of negative θ_{CW}. The strong antiferromagnetic interaction is at the heart of the realization of many novel quantum states, such as unconventional superconductivity,[22,28] magnetic frustrations,[73–75] *etc.* Given the lack of long-range magnetic order down to 1.8 K, the spin of this system can also be considered highly frustrated and warrants future investigations.

The resistivity of $Y_4Fe_xGe_8$ exhibits a typical metallic behavior with a residual-resistance-ratio (RRR = R_{250K}/R_{10K}) of 1.97 (Fig. 6b). The relatively small RRR ratio may result from scattering related to the large disorder on the Fe-site. A possible consequence of this disorder is the apparent saturation in the temperature dependence of the resistivity near room temperature at a value of 57 μΩ cm. This behavior resembles the approach to the Ioffe–Regel limit observed in disordered systems.[76] For example, in A15 compounds (intermetallics with Cr_3Si structure type), limiting resistivities of around

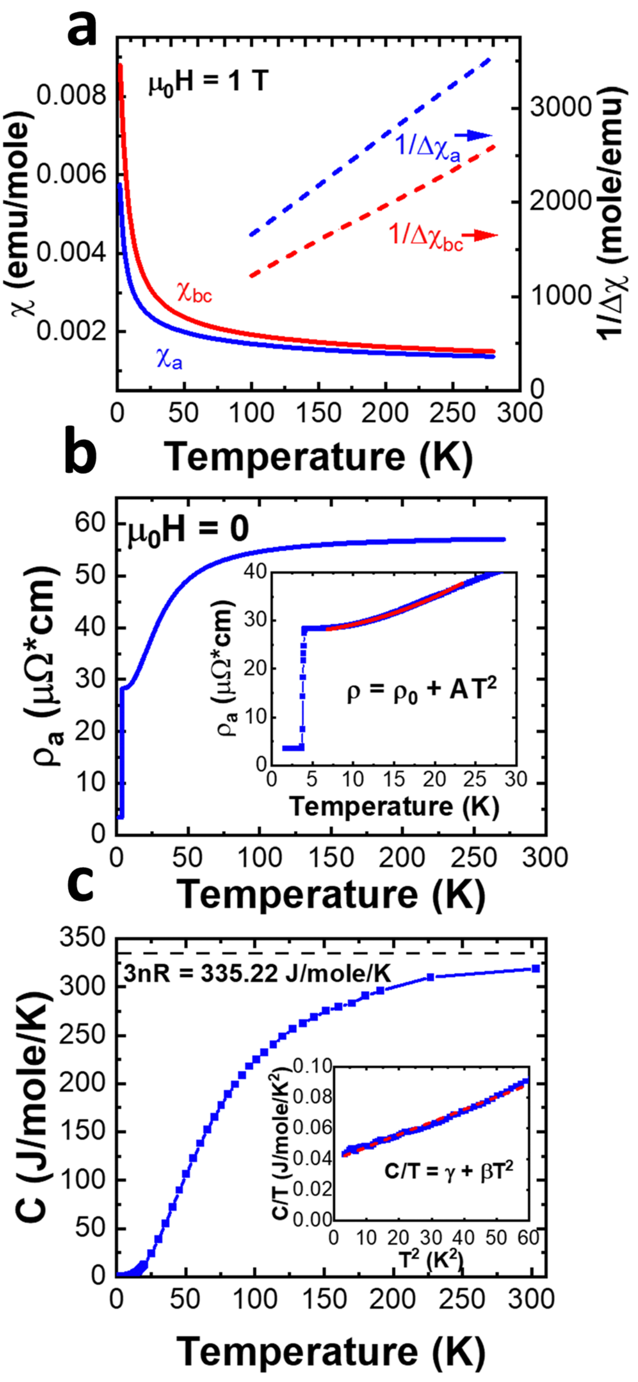

Fig. 6 Characterization of heavy fermion behavior in $Y_4Fe_xGe_8$. The T-dependence of (a) χ_a and χ_{bc} (left scale) along with $\Delta\chi_a^{-1}$ and $\Delta\chi_{bc}^{-1}$ (right scale) with μ_0H = 1 T; (b) electrical resistivity ρ_a and (b) inset a zoomed-in view with $\rho = \rho_0 + AT^2$ fitting curve; (c) heat capacity $C(T)$ and (c) inset a zoomed-in view with $C(T) = \gamma T + \beta T^3$ fitting curve.

100–150 μΩ cm have been reported.[76] At temperatures below ∼25 K, the system behaves as a Fermi-liquid[77–79] with resistivity following a T^2 temperature dependence $\rho(T) = \rho_0 + AT^2$, where ρ_0 = 27.3 μΩ cm and A = 0.019 μΩ cm K^{-2} (Fig. 6b inset).

Lastly, heat capacity measured down to 1.8 K reveals no obvious anomalies resembling any transitions (Fig. 6c). The low-temperature heat capacity can be well described by $C(T) = \gamma T + \beta T^3$ where γ and β is the Sommerfeld coefficient and the Debye constant representing the contribution from electron and phonon, respectively (Fig. 6c inset). The Debye constant β = 0.81 mJ $mole^{-1}$ K^{-4} leads to a Debye temperature of 314.5 K, consistent with the observation that the heat capacity approaches the Dulong–Petit limit near room temperature. Meanwhile, the Sommerfeld coefficient, γ, is estimated to be 39.8 mJ $mole^{-1}$ K^{-2}, which is large even for a metallic system, suggesting enhanced electronic correlation and heavy fermion behavior.

To further explore this enhanced electronic correlation, we carried out DFT calculations for $Y_4Fe_xGe_8$ with x = 1.5 using a $\sqrt{2} \times \sqrt{2}$ supercell of the orthorhombic *Cmcm* space group structure. We adopt Vienna ab initio simulation package (VASP)[80,81] to compute the DFT band structure using the Perdew–Burke–Ernzerhof (PBE)[82] correlation energy functional. We used the 8 × 8 × 4 *k*-mesh along with the energy cutoff of 400 eV for the plane-wave basis. Due to computational limitations, a structure with partial vacancy could not be modeled with DFT. Thus, we used this $\sqrt{2} \times \sqrt{2}$ supercell with a formula of $Y_4Fe_{1.5}Ge_8$ to carry out DFT calculations. The detailed atomic coordinates of the relaxed structure are described in Table S4 (ESI†). Indeed, our DFT calculation displays both flat bands of the Fe 3d state close to the Fermi level (Fig. 7a red color) and the large density of states (DOS) below the Fermi level (Fig. 7c), which is consistent with the large value of γ, suggesting a heavy fermion behavior. The apparent flatness of Fe d bands originates from the small hopping between Fe ions induced by the large in-plane Fe–Fe distance (∼5.77 Å) due to the Fe vacancies. The orbital-resolved DOS shows mostly the Fe 3d and Ge 4p characters below the Fermi level while the Y d state is located at higher energy above the Fermi level. This feature tends to lead to possible electronic instability such as ferromagnetism, known as the Stoner's criterion for magnetism,[83] and is consistent with the heavy fermion behavior we observed in this system. Furthermore, the significant hybridization between Fe 3d and Ge 4p orbitals, which is evident in the mixed nature of these states in the band structure near the Fermi level, also has the potential to trigger heavy fermion behavior in the localized Fe d orbitals.

In addition to the DFT calculation, the heavy fermion is further evidenced by two empirical dimensionless ratios. By examining the Kadowaki–Woods ratio (KWR), we can gain insights into the nature of electron–electron interactions in the material. The Kadowaki–Woods ratio is defined as KWR = A/γ^2, where A is the coefficient of the quadratic term in the temperature dependence of electrical resistivity, which is experimentally observed when the electron–electron scattering is dominating over the electron–phonon scattering and γ is the Sommerfeld coefficient accounting electronic contribution to the specific heat. This ratio helps identify the presence of heavy fermion behavior by quantifying the relationship between the electronic specific heat coefficient (γ) and the electrical resistivity (ρ). Empirically, even though both A and γ^2 vary by order of magnitude across the materials, their ratio converges to 0.04 × 10^{-5} μΩ cm $mole^2$ K^2 mJ^{-2} for normal d-band metals

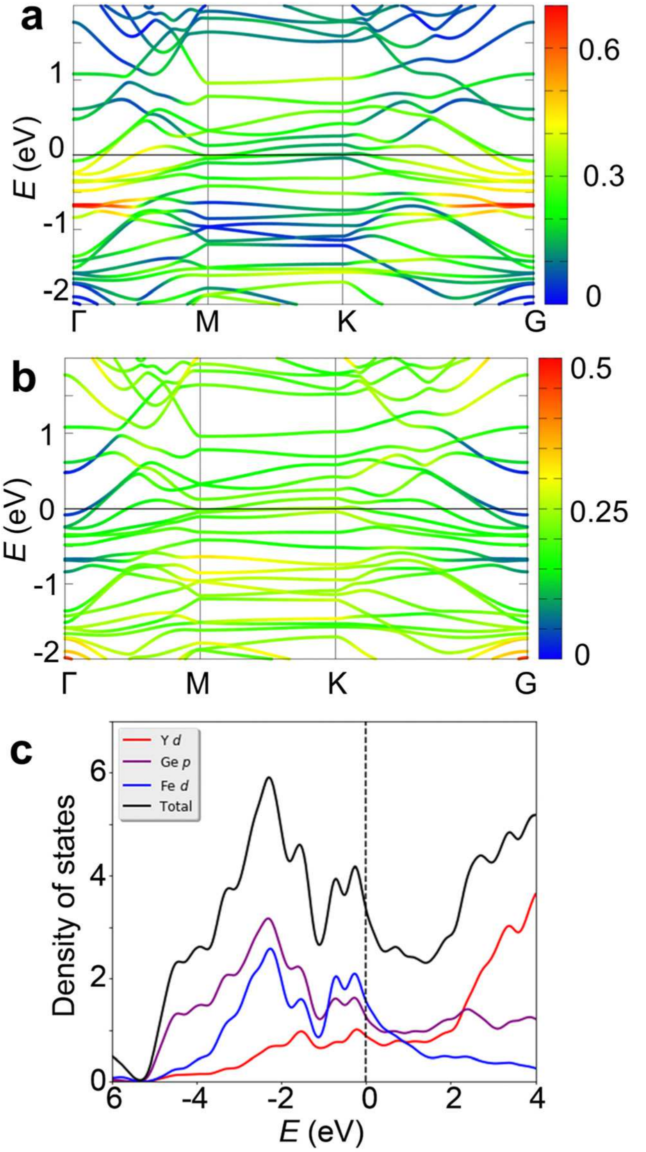

Fig. 7 Density functional theory calculations of $Y_4Fe_{1.5}Ge_8$ (for x = 1.5 using a supercell) with band structures showing projections of (a) Fe 3d electrons and (b) Ge 4p electrons and (c) density of states (DOS). The color scheme of the bands shown in (a) and (b) corresponds to the DOS of Fe 3d electrons and Ge 4p, respectively.

and 1.0×10^{-5} μΩ cm mole^2 K^2 mJ^{-2} for heavy-fermion systems.[19,78,79] Adopting A and γ values estimated above, the KWR of $A/\gamma^2 = 1.2 \times 10^{-5}$ μΩ cm mole^2 K^2 mJ^{-2} falls near the value typically seen for a heavy fermion system, providing another evidence reaffirming the heavy fermion behavior in the $Y_4Fe_xGe_8$.

In addition, combining magnetic susceptibility and heat capacity results, another informative ratio that can be estimated the is Wilson ratio (WR),[84] $\mathrm{WR} = \pi^2 k_B{}^2 \chi_0/(3\mu_B{}^2\gamma)$, where χ_0 is the Pauli magnetic susceptibility and γ is the Sommerfeld coefficient. Both χ_0 and γ are related to the electronic density of state near the Fermi surface and the dimensionless Wilson ratio between them reflects the degree of correlations between electrons and spins.[85–87] For example, a Wilson ratio greater than unity indicates enhanced electronic correlations, while a ratio close to or less than unity suggests weaker or absence of correlations. Using the Pauli magnetic susceptibility estimated from the high-temperature Curie–Weiss analysis, the WR reaches 1.83, which is close to the value of 2 for strongly correlated systems in contrast to the value of 1 for the non-correlated systems.[85–87] Overall, the Wilson ratio analysis strongly indicates that the electrons in $Y_4Fe_xGe_8$ are strongly correlated, consistent with the strong antiferromagnetic coupling suggested by the magnetic susceptibility measurements and the heavy fermion state discussed above. It is worth mentioning that strong antiferromagnetic coupling and the absence of a long-range magnetic order were also observed in another heavy fermion metal system $FeSi_{1-x}Al_x$.[52] Interestingly, the coexistence of heavy fermion behavior and strong AFM spin fluctuations due to spin frustration resembles the celebrated LiV_2O_4,[37–42] providing $Y_4Fe_xGe_8$ as another possible archetype for the study of heavy fermion systems originating from unconventional non-Kondo mechanisms.

Possible superconductivity

We observed a sharp transition near $T_c \sim 3.5$ K evidenced in both the magnetic susceptibility (Fig. 8a) and the resistivity (Fig. 8b). In addition, the transition moves to lower temperatures with an increasing magnetic field, an anticipated behavior for a superconductor as the magnetic flux breaks Cooper pairs. However, the low superconducting volume fraction, the non-zero residual resistance, and the lack of heat capacity anomaly all suggest that the superconducting transition observed is not in the bulk. Moreover, the proximity of the observed T_c to the superconducting transition temperature of indium (T_c(In) = 3.4 K) further hinders the justification of the superconducting state in the $Y_4Fe_xGe_8$. Therefore, we extended our measurement temperature range down to the milli-Kelvin range.

As shown in Fig. 8(d), an additional 64% drop of resistivity is observed between 3 K and 0.05 K with an onset temperature of 2.2 K. This additional resistivity drop comes entirely from the $Y_4Fe_xGe_8$ itself as residual indium, if there is any, already becomes a superconductor under this condition and has no resistivity contribution. In addition, the estimated upper critical field of 600 Oe (Fig. 8(d) inset) is also higher than that of indium (H_c(In) = 286 Oe), further highlighting contributions from $Y_4Fe_xGe_8$ itself. Similarly, the onset of resistivity drops with an increasing magnetic field, suggesting a superconducting transition onset, but the non-zero residual resistivity and the broad transition once again hinder the claim of bulk superconductivity in the $Y_4Fe_xGe_8$. One possible extrinsic explanation of this superconducting-like behavior is that a thin layer of YGe_3, which is a superconductor with zero resistivity below 2.2 K,[88] intergrow with single crystal $Y_4Fe_xGe_8$. However, we deem this scenario unlikely because of the very different way of stacking along the b-axis and a large lattice mismatch along the ac-plane. The broad transition under a zero magnetic field is another piece of evidence that this extrinsic scenario is

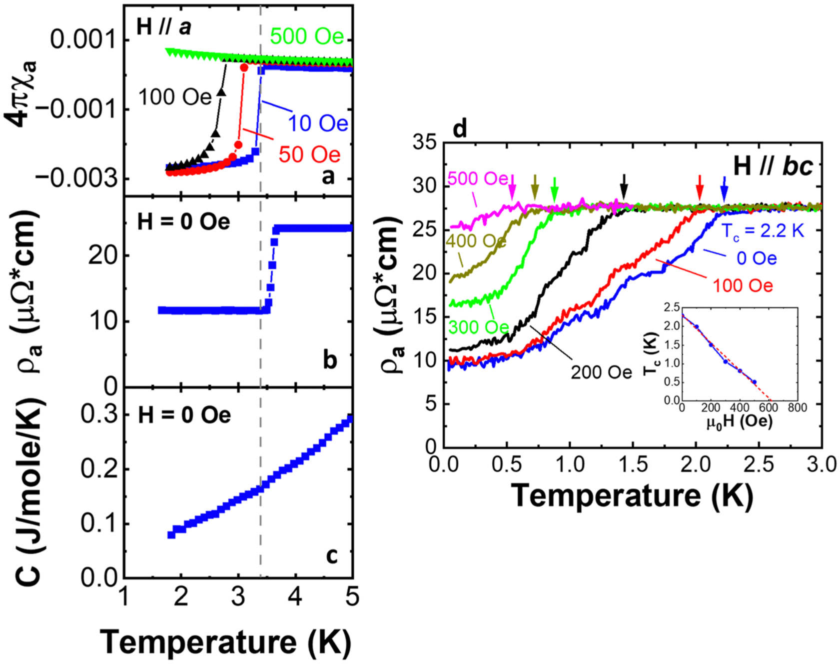

Fig. 8 Characterization of possible superconductivity. The T-dependence of (a) $4\pi\chi_a$ under various applied fields; (b) electrical resistivity ρ_a; (c) heat capacity $C(T)$. Note a grey dashed line near the transition onset is used as a guide for the eye. (d) Electrical resistivity ρ_a down to milli-Kelvin under various fields. (d) Inset: Field dependence of the transition onset.

doubtful. As discussed previously, the wide range of Fe-content, x, has been demonstrated in single- and powder-crystal X-ray diffraction, and its large inhomogeneity even at the atomic level is well established from the above-presented HRTEM studies. Accordingly, we speculate that the $Y_4Fe_xGe_8$ might indeed be an intrinsic bulk superconductor but with a T_c highly sensitive to the amount of Fe within its structure. This postulated scenario can explain both the broad transition and non-zero residual resistivity due to the inhomogeneity of Fe across the single crystal of $Y_4Fe_xGe_8$ well. In addition, our magnetic susceptibility measurements on the powder samples synthesized *via* the direct combination method (without the use of indium in the synthesis) also suggest the x-dependent diamagnetic response on the low-Fe side of the phase diagram (Fig. S6, ESI†).

Conclusions

We uncovered a partial order of Fe-vacancies with asymmetrical distortions and distorted Ge square-net in a series of Fe-deficient $Y_4Fe_xGe_8$ ($1 \leq x \leq 1.5$) compounds and used solid-state reactions with different Fe ratios to show that the stoichiometric $YFeGe_2$ of the $CeNiSi_2$-type reported in literature belonged to the same Fe-deficient group described in this work. With the use of advanced structural characterizations using X-ray diffraction and high-resolution electron microscopy we probed the limits of Fe content, which does not seem to reach $x = 4$. Our findings highlight the necessity for more rigorous examination of crystal structures in the $CeNiSi_2$-family, as similar nonstoichiometries and partial occupancies are likely present in most members of this group. Interestingly, $Y_4Fe_xGe_8$ exhibits heavy fermion behavior, which is uncommon for a 3d transition metal intermetallic without f electrons. This behavior, combined with strong spin fluctuations, suggests an unconventional non-Kondo mechanism related to spin fluctuation. This discovery opens avenues for exploring heavy fermion systems induced by 3d transition metals through non-Kondo mechanisms related to strong spin fluctuations, particularly in RMX_2 and related intermetallic compounds. Moreover, a possible superconductivity that is highly sensitive to the Fe-content also hints at the possibility of unconventional superconductivity. As the RMX_2 system is capable of hosting a large number of transition metals across 3d, 4d and 5d elements and adopt tunable distorted structures induced by size effects in the different X = Si, Ge and Sn members of the family, we can expect that they can be leveraged to design strongly electron-correlated systems in which to investigate competing interactions and other emergent phenomena.

Author contributions

The work was conceived by H. Z., X. Z., M. U., D.-Y. C., and M. G. K., with input from all authors. H. Z., X. Z., and M. U. carried out the synthesis, lab X-ray diffraction, and elemental analysis. H. Z., X. Z., and Y.-S. C. carried out synchrotron X-ray diffraction and data analysis. H. Z. performed resistivity, magnetization, and heat capacity measurements. L. Y. and J. W. collected and analyzed high-resolution transmission electron microscopy data. P. E. M. collected and analyzed X-ray photoelectron spectroscopy data. H. P. performed first-principle calculations. A. P. D. collected and analyzed Mössbauer

Spectroscopy. R. C. and U. W. performed electrical transport down to milli-Kelvin and contributed magnetization measurements. S. R., D.-Y. C., and M. G. K. supervised the project. H. Z., X. Z., D.-Y. C., and M. G. K. wrote the manuscript with input from all authors.

Data availability

Additional elemental analysis and X-ray photoelectron spectroscopy, single crystal diffraction data, photoemission yield spectroscopy in air measurement of work function, and additional magnetic susceptibility measurements on powder samples synthesized *via* direct combination method. Additional crystallographic information files (CIFs): CSD# 2357729 and 2357730.†

Conflicts of interest

The authors declare no competing financial interest.

Acknowledgements

This work is primarily supported by the U.S. Department of Energy, Office of Science, Basic Energy Sciences, Materials Sciences, and the Engineering Division. This material is based upon work supported by Laboratory Directed Research and Development (LDRD) funding from Argonne National Laboratory, provided by the Director, Office of Science, of the U.S. Department of Energy under Contract No. DE-AC02-06CH11357. The work (SEM/EDX and TEM) performed at the Center for Nanoscale Materials, a U.S. Department of Energy Office of Science User Facility, was supported by the U.S. DOE, Office of Basic Energy Sciences, under Contract No. DE-AC02-06CH11357. Work at the beamline 15-IDD at the Advanced Photon Source (APS) at Argonne National Laboratory was supported by the U.S. Department of Energy, Office of Science, Office of Basic Energy Sciences under Contract No. DE-AC02-06CH11357. NSF's ChemMatCARS Sector 15 is supported by the Divisions of Chemistry (CHE) and Materials Research (DMR), National Science Foundation, under grant number NSF/CHE-2335833 and NSF/CHE-1834750. H. Park acknowledges the computing resources provided by Bebop, a high-performance computing cluster operated by the Laboratory Computing Resource Center at Argonne National Laboratory. XPS measurements were conducted in the EPIC facility of Northwestern University's NUANCE Center, which has received support from the SHyNE Resource (NSF ECCS-2025633), the International Institute of Nanotechnology (IIN), and Northwestern's MRSEC program (NSF DMR-2308691). We thank Isaiah Gilley for providing photoemission yield spectroscopy in air measurements.

References

1 O. Bodak and E. Gladyshevsky, *Kristallografiya*, 1969, **14**, 990–994.
2 R.-D. Hoffmann and R. Pöttgen, *Z. Kristallogr. - Cryst. Mater.*, 2001, **216**, 127–145.
3 G. Venturini, M. François, B. Malaman and B. Roques, *J. Less-Common Met.*, 1990, **160**, 215–228.
4 H. Bie, A. V. Tkachuk and A. Mar, *J. Solid State Chem.*, 2009, **182**, 122–128.
5 L. Gustin, L. Xing, M. T. Pan, R. Jin and W. Xie, *J. Alloys Compd.*, 2018, **741**, 840–846.
6 V. Mykhalichko, R. Kozak and R. Gladyshevskii, *Chem. Met. Alloys*, 2015, 55–62.
7 M. A. Zhuravleva, D. Bilc, R. J. Pcionek, S. D. Mahanti and M. G. Kanatzidis, *Inorg. Chem.*, 2005, **44**, 2177–2188.
8 J.-K. Bao, H. Zheng, J. Wen, S. Ramakrishnan, H. Zheng, J. S. Jiang, D. Bugaris, G. Cao, D. Y. Chung, S. van Smaalen and M. G. Kanatzidis, *Chem. Mater.*, 2021, **33**, 7839–7847.
9 A. Weiland, J. B. Felder, G. T. McCandless and J. Y. Chan, *Chem. Mater.*, 2020, **32**, 1575–1580.
10 T. M. Kyrk, M. Bravo, G. T. McCandless, S. H. Lapidus and J. Y. Chan, *ACS Omega*, 2022, **7**, 19048–19057.
11 B. Chevalier, P. Lejay, J. Etourneau and P. Hagenmuller, *Mater. Res. Bull.*, 1983, **18**, 315–330.
12 W. H. Lee, K. S. Kwan, P. Klavins and R. N. Shelton, *Phys. Rev. B: Condens. Matter Mater. Phys.*, 1990, **42**, 6542–6545.
13 A. M. Alsmadi, H. Nakotte, J. L. Sarrao, M. H. Jung and A. H. Lacerda, *J. Appl. Phys.*, 2003, **93**, 8343–8345.
14 T. Nakano, M. Ohashi, G. Oomi, K. Matsubayashi and Y. Uwatoko, *Phys. Rev. B: Condens. Matter Mater. Phys.*, 2009, **79**, 172507.
15 Y. Hirose, N. Nishimura, F. Honda, K. Sugiyama, M. Hagiwara, K. Kindo, T. Takeuchi, E. Yamamoto, Y. Haga, M. Matsuura, K. Hirota, A. Yasui, H. Yamagami, R. Settai and Y. Ōnuki, *J. Phys. Soc. Jpn.*, 2011, **80**, 024711.
16 S. Doniach, *Phys. B+C*, 1977, **91**, 231–234.
17 H. v Löhneysen, A. Rosch, M. Vojta and P. Wölfle, *Rev. Mod. Phys.*, 2007, **79**, 1015.
18 Q. Si and F. Steglich, *Science*, 2010, **329**, 1161–1166.
19 G. R. Stewart, *Rev. Mod. Phys.*, 1984, **56**, 755–787.
20 N. Mathur, F. Grosche, S. Julian, I. Walker, D. Freye, R. Haselwimmer and G. Lonzarich, *Nature*, 1998, **394**, 39–43.
21 B. White, J. Thompson and M. Maple, *Phys. C*, 2015, **514**, 246–278.
22 Y. Kamihara, T. Watanabe, M. Hirano and H. Hosono, *J. Am. Chem. Soc.*, 2008, **130**, 3296–3297.
23 J. Paglione and R. L. Greene, *Nat. Phys.*, 2010, **6**, 645–658.
24 A. D. Christianson, E. A. Goremychkin, R. Osborn, S. Rosenkranz, M. D. Lumsden, C. D. Malliakas, I. S. Todorov, H. Claus, D. Y. Chung, M. G. Kanatzidis, R. I. Bewley and T. Guidi, *Nature*, 2008, **456**, 930–932.
25 D. C. Johnston, *Adv. Phys.*, 2010, **59**, 803–1061.
26 P. Hirschfeld, M. Korshunov and I. Mazin, *Rep. Prog. Phys.*, 2011, **74**, 124508.
27 R. M. Fernandes, A. I. Coldea, H. Ding, I. R. Fisher, P. Hirschfeld and G. Kotliar, *Nature*, 2022, **601**, 35–44.
28 J. G. Bednorz and K. A. Müller, *Z. Phys. B Condens. Matter*, 1986, **64**, 189–193.

29 Z.-H. Cui, H. Zhai, X. Zhang and G. K.-L. Chan, *Science*, 2022, **377**, 1192–1198.

30 J. Guo, S. Jin, G. Wang, S. Wang, K. Zhu, T. Zhou, M. He and X. Chen, *Phys. Rev. B: Condens. Matter Mater. Phys.*, 2010, **82**, 180520.

31 J. Chen, K. Semeniuk, Z. Feng, P. Reiss, P. Brown, Y. Zou, P. W. Logg, G. I. Lampronti and F. M. Grosche, *Phys. Rev. Lett.*, 2016, **116**, 127001.

32 H. Kim, S. Ran, E. D. Mun, H. Hodovanets, M. A. Tanatar, R. Prozorov, S. L. Bud'ko and P. C. Canfield, *Philos. Mag.*, 2015, **95**, 804–818.

33 Y. Zou, Z. Feng, P. W. Logg, J. Chen, G. Lampronti and F. M. Grosche, *Phys. Status Solidi RRL*, 2014, **8**, 928–930.

34 D. J. Singh, *Phys. Rev. B: Condens. Matter Mater. Phys.*, 2014, **89**, 024505.

35 V. K. Pecharskii, O. Y. Mruz, M. B. Konyk, P. S. Salamakha, P. K. Starodub, M. F. Fedyna and O. I. Bodak, *J. Struct. Chem.*, 1989, **30**, 777–782.

36 S. Kondo, D. Johnston, C. Swenson, F. Borsa, A. Mahajan, L. Miller, T. Gu, A. Goldman, M. Maple and D. Gajewski, *Phys. Rev. Lett.*, 1997, **78**, 3729.

37 O. Chmaissem, J. Jorgensen, S. Kondo and D. Johnston, *Phys. Rev. Lett.*, 1997, **79**, 4866.

38 V. Eyert, K.-H. Höck, S. Horn, A. Loidl and P. S. Riseborough, *Europhys. Lett.*, 1999, **46**, 762.

39 J. Matsuno, A. Fujimori and L. Mattheiss, *Phys. Rev. B: Condens. Matter Mater. Phys.*, 1999, **60**, 1607.

40 C. Urano, M. Nohara, S. Kondo, F. Sakai, H. Takagi, T. Shiraki and T. Okubo, *Phys. Rev. Lett.*, 2000, **85**, 1052.

41 J. Hopkinson and P. Coleman, *Phys. Rev. Lett.*, 2002, **89**, 267201.

42 S. Burdin, D. Grempel and A. Georges, *Phys. Rev. B: Condens. Matter Mater. Phys.*, 2002, **66**, 045111.

43 W. Kobayashi, I. Terasaki, J.-I. Takeya, I. Tsukada and Y. Ando, *J. Phys. Soc. Jpn.*, 2004, **73**, 2373–2376.

44 H. Zhao, Y. Zhang, P. Schlottmann, R. Nandkishore, L. E. DeLong and G. Cao, *Phys. Rev. Lett.*, 2024, **132**, 226503.

45 Y. Zhang, H. Lu, X. Zhu, S. Tan, W. Feng, Q. Liu, W. Zhang, Q. Chen, Y. Liu and X. Luo, *Sci. Adv.*, 2018, **4**, eaao6791.

46 J. R. Neilson and T. M. McQueen, *J. Am. Chem. Soc.*, 2012, **134**, 7750–7757.

47 C. Pfleiderer, M. Uhlarz, S. Hayden, R. Vollmer, H. V. Löhneysen, N. Bernhoeft and G. Lonzarich, *Nature*, 2001, **412**, 58–61.

48 S. Yates, G. Santi, S. Hayden, P. Meeson and S. Dugdale, *Phys. Rev. Lett.*, 2003, **90**, 057003.

49 V. Vaňo, M. Amini, S. C. Ganguli, G. Chen, J. L. Lado, S. Kezilebieke and P. Liljeroth, *Nature*, 2021, **599**, 582–586.

50 L. Crippa, H. Bae, P. Wunderlich, I. I. Mazin, B. Yan, G. Sangiovanni, T. Wehling and R. Valentí, *Nat. Commun.*, 2024, **15**, 1357.

51 W. Zhao, B. Shen, Z. Tao, Z. Han, K. Kang, K. Watanabe, T. Taniguchi, K. F. Mak and J. Shan, *Nature*, 2023, **616**, 61–65.

52 J. DiTusa, K. Friemelt, E. Bucher, G. Aeppli and A. Ramirez, *Phys. Rev. B: Condens. Matter Mater. Phys.*, 1998, **58**, 10288.

53 P. Sun, N. Oeschler, S. Johnsen, B. B. Iversen and F. Steglich, *Dalton Trans.*, 2010, **39**, 1012–1019.

54 K. Umeo, Y. Hadano, S. Narazu, T. Onimaru, M. A. Avila and T. Takabatake, *Phys. Rev. B: Condens. Matter Mater. Phys.*, 2012, **86**, 144421.

55 A. Ramires and J. L. Lado, *Phys. Rev. Lett.*, 2021, **127**, 026401.

56 Y.-Z. Chou and S. D. Sarma, *Phys. Rev. Lett.*, 2023, **131**, 026501.

57 Z.-D. Song and B. A. Bernevig, *Phys. Rev. Lett.*, 2022, **129**, 047601.

58 G. Sheldrick, *Acta Crystallogr., Sect. A: Found. Crystallogr.*, 2015, **71**, 3–8.

59 G. Sheldrick, *Acta Crystallogr., Sect. C: Struct. Chem.*, 2015, **71**, 3–8.

60 O. V. Dolomanov, L. J. Bourhis, R. J. Gildea, J. A. K. Howard and H. Puschmann, *J. Appl. Crystallogr.*, 2009, **42**, 339–341.

61 A. P. Douvalis, A. Polymeros and T. Bakas, *J. Phys.: Conf. Ser.*, 2010, **217**, 012014.

62 H. H. Hamdeh, M. R. Al-Hilali, N. S. Dixon and L. S. Fritz, *Phys. Rev. B: Condens. Matter Mater. Phys.*, 1992, **45**, 2201–2206.

63 N. Greenwood and T. Gibb, *Mössbauer Spectrosc.*, 1971, 1–16.

64 J. B. Forsyth, C. E. Johnson and P. J. Brown, *Philos. Mag. (1798–1977)*, 1964, **10**, 713–721.

65 G. Fabri, E. Germagnoli, M. Musci and V. Svelto, *Phys. Rev.*, 1965, **138**, A178–A179.

66 O. Massenet and H. Daver, *Solid State Commun.*, 1977, **21**, 37–40.

67 Y. Endoh, K. Yamada, J. Beille, D. Bloch, H. Endo, K. Tamura and J. Fukushima, *Solid State Commun.*, 1976, **18**, 735–737.

68 T.-C. Lin, G. Seshadri and J. A. Kelber, *Appl. Surf. Sci.*, 1997, **119**, 83–92.

69 M. C. Biesinger, B. P. Payne, A. P. Grosvenor, L. W. Lau, A. R. Gerson and R. S. C. Smart, *Appl. Surf. Sci.*, 2011, **257**, 2717–2730.

70 W. Mi, Y. Liu, E. Jiang and H. Bai, *J. Appl. Phys.*, 2008, **103**, 093713.

71 G. A. Lungu, N. G. Apostol, L. E. Stoflea, R. M. Costescu, D. G. Popescu and C. M. Teodorescu, *Materials*, 2013, **6**, 612–625.

72 J. Liu, X. Cheng, F. Tong and X. Miao, *J. Alloys Compd.*, 2015, **650**, 70–74.

73 L. Savary and L. Balents, *Rep. Prog. Phys.*, 2016, **80**, 016502.

74 Y. Zhou, K. Kanoda and T.-K. Ng, *Rev. Mod. Phys.*, 2017, **89**, 025003.

75 C. Broholm, R. Cava, S. Kivelson, D. Nocera, M. Norman and T. Senthil, *Science*, 2020, **367**, eaay0668.

76 N. Hussey, K. Takenaka and H. Takagi, *Philos. Mag.*, 2004, **84**, 2847–2864.

77 L. D. Landau, *J. Exp. Theor. Phys.*, 1957, **3**, 920.

78 K. Kadowaki and S. Woods, *Solid State Commun.*, 1986, **58**, 507–509.

79 A. Jacko, J. Fjærestad and B. Powell, *Nat. Phys.*, 2009, **5**, 422–425.

80 G. Kresse and J. Furthmüller, *Phys. Rev. B: Condens. Matter Mater. Phys.*, 1996, **54**, 11169–11186.

81 G. Kresse and D. Joubert, *Phys. Rev. B: Condens. Matter Mater. Phys.*, 1999, **59**, 1758–1775.

82 J. P. Perdew, A. Ruzsinszky, G. I. Csonka, O. A. Vydrov, G. E. Scuseria, L. A. Constantin, X. Zhou and K. Burke, *Phys. Rev. Lett.*, 2008, **100**, 136406.

83 E. C. Stoner, *Proc. R. Soc. London, Ser. A*, 1938, **165**, 372–414.

84 K. G. Wilson, *Rev. Mod. Phys.*, 1975, **47**, 773.

85 L. Balents, *Nature*, 2010, **464**, 199–208.

86 T. Usuki, N. Kawakami and A. Okiji, *Phys. Lett. A*, 1989, **135**, 476–480.

87 X.-W. Guan, X.-G. Yin, A. Foerster, M. T. Batchelor, C.-H. Lee and H.-Q. Lin, *Phys. Rev. Lett.*, 2013, **111**, 130401.

88 M. Wei, H. Sung and W. Lee, *Phys. C*, 2005, **424** 25–28.